To cite this version :

Effects of the impact of a low temperature nitrogen jet on metallic surfaces

By H. Laribou[1],*, C. Fressengeas[1], D. Entemeyer[1], V. Jeanclaude[1], R. Pesci[1] and A. Tazibt[2]

[1]*Laboratoire d'Etude des Microstructures et de Mécanique des Matériaux (LEM3), Université de Lorraine/CNRS, Ile du Saulcy, Metz 57045, France*
[2]*CRITT TJF&U, Laboratoire Jet Fluide Très Hautes Pressions, Bar-le-Duc 55000, France*

The technology of nitrogen jets impacting surfaces at low temperature has recently been introduced for surface cleaning/stripping. Under the impact of the jet, the material surface undergoes a thermomechanical shock inducing complex transformation mechanisms. Depending on the material and test parameters such as standoff distance, dwell time, upstream pressure, the latter include cleavage, cracking, spalling, blistering, grain fragmentation, phase transformation and ductile deformation. Quite often, these modes are superimposed in the same test, or even in the same material area. In this study, an overview of these mechanisms is proposed for metallic materials. Measurements of thermomechanical variables in the impacted area are presented and the influence of the test parameters on surface transformation is investigated. Grain fragmentation and ultrafast transport of nitrogen in a deep layer below the surface are explored.

Keywords: nitrogen jet; impact on surface; stripping; thermoelastic wave; surface damage; surface removal

1. Introduction

A new technology for surface stripping or cleaning has recently been developed using a nitrogen jet under high containment pressure and low temperature. This process is presented as an environmentally friendly technology, when compared with conventional methods such as chemical stripping, high pressure water jet cleaning or sand blasting, because it does not generate additional waste and releases neutral gas into the atmosphere. The process consists of impacting onto a material surface a low temperature jet obtained by releasing the liquid (or hypercritical) nitrogen stored in a high-pressure vessel (e.g. 300 MPa) through a nozzle with an outlet temperature of approximately 150 K. In this study, we were interested in the interactions of the nitrogen jet with the surface of the targeted material, with focus on possible material damage or surface treatment. To the best of our knowledge, the international literature is silent on this topic. Earlier published work on nitrogen jets has essentially focused on heat transfer properties (Dreitser *et al.* 2001). By analogy and as a first

approach, it may have been tempting to extrapolate to the case of nitrogen jets the surface damage mechanisms owing to water jets under high pressure, or to cryogenic carbonic gas jets. However, the thermomechanical conditions in the impacted area, i.e. pressure, temperature, jet velocity, phase composition, are rather different. Furthermore, the interaction jet/matter involves a fairly large number of parameters, such as upstream data (vessel pressure, nozzle geometry, mass flow rate, etc.), test variables (standoff distance, dwell time, etc.), and the characteristics of the targeted material (surface roughness, thermomechanical properties, etc.). These various factors can combine to produce a large variety of interaction modes with the targeted surface. In addition, several effects of the thermomechanical shock undergone by the material surface area may also combine. For example, quickly reducing the temperature may promote material brittleness, while the induced thermoelastic tension waves may cause crack nucleation and growth. In the meantime, depressurization of the cryogenic nitrogen during vaporization at the surface may induce a blasting effect, which may in turn result in plastic deformation and material lifting, while cavitations of gas inclusions into droplets may induce high pressure impacts and crater formation. In the presence of such a diversity of jet/surface interaction modes, this study focuses on metallic surfaces. Its first aim is to present experimental evidence of the complex phenomena at work in such an involved environment, and to differentiate them from more conventional patterns. Measurements of thermomechanical parameters of the jet in the impacted area (impact force, temperature, velocity, mass density, etc.), are presented, and quantitative estimates of the stress level involved in the various jet/surface interaction mechanisms are provided. Surface hardening through grain fragmentation and nitrogen transport in a certain layer below the surface are also explored. The paper is organized as follows. Section 2 presents the experimental setup, and the measurements performed for an evaluation of the jet characteristics at impact. Section 3 presents the experimental results obtained in several materials (steels, copper and an aluminium alloy). These results are discussed in §4 in order to ascertain the jet/surface interaction mechanisms. Concluding remarks are provided in §5.

2. Experimental section

(a) Nitrogen jet generation

The setup for nitrogen jet generation has been produced by the American company NitroCision since 2003. The delivery system involves two stages of pumps and heat exchangers to create a high velocity cryogenic jet stream. The pressure in the intensifier before delivery in the atmosphere can be as high as 300 MPa. Release into the atmosphere occurs through a nozzle, where the nitrogen gas acquires supersonic velocity. Throughout this work, the nozzle diameter is considered to be 0.2 mm. Dynamic simulations of a single-phase compressible fluid suggest that, during its flight time before impacting the target, the jet undergoes supersonic–subsonic transition through a Mach disc, while its static pressure decreases to nearly the atmospheric pressure level (Dubs *et al.* 2011). In the meantime, there are strong indications from this work, as well as from

experiments reported below, that re-condensation occurs and that the jet at impact is in a dense multi-phase state, possibly including hypercritical fluid, liquid and solid pellets.

(b) Temperature measurements

A cast steel plate $(200 \times 100 \, \text{mm}^2)$ was used to measure the temperature in the impacted area. The plate was equipped with a T-type thermocouple (with a sensitivity of approx. $39 \, \mu\text{V}/°\text{C}$) laid out at a depth of $0.5 \, \text{mm}$ below the impact point. The jet was quickly displaced into the measurement area, where it remained steady during the duration of the measurements. After a transient stage showing fast temperature decrease, a steady-state temperature was obtained, indicating thermal equilibrium of the thermocouple with its environment. Since the heat capacity of the steel plate is relatively low, this temperature is fairly representative of the jet temperature. It decreases with the operating vessel pressure, and its minimum value is approximately $-115°\text{C}$ in the present experiments. We note that using perfectly insulated upstream conducts for the nitrogen flow could lead to even lower temperatures.

(c) Measurement of the force impinged on the work piece surface

Series of measurements were performed, in order to quantify the impact force of the nitrogen jet on the work piece surface. Together with measurements of the mass flow rate, the obtained data are useful for inferring the thermo-physical state of the jet prior to impact. The impact force was measured by using a calibrated force sensor U93/1 kN (weakly sensitive to the temperature with a maximum ± 0.5 per cent variation with respect to the nominal sensitivity, and thermally protected from the jet). For an upstream pressure of $210 \, \text{MPa}$, the average impact force amounts to a modest $11 \, \text{N}$ at a $120 \, \text{mm}$ standoff distance, and it shows a 10 per cent decrease as the standoff distance increases from 20 to $140 \, \text{mm}$. Small irregularities about the average value are owing to pulsations of the operating system, which induce nearly periodic oscillations in the jet velocity and external surface. The impact force F relates to the mass flow rate $\dot{m}$ according to the relation:

$$F = \dot{m}U, \quad \dot{m} = \rho S U, \tag{2.1}$$

where ρ is the average nitrogen mass density, S the jet cross-section area and U its average velocity over a section close to the impacted surface, in the subsonic range. Hence, this velocity can be estimated from the measurement of the impact force and the value of the mass flow rate delivered by the system. From our data on the nitrogen consumption in the experimental setup, the mass flow rate is slightly larger than $80 \, \text{g s}^{-1}$ (owing to various loss rates in the atmosphere). If we adopt the value $\dot{m} = 90 \, \text{g s}^{-1}$ the jet velocity U turns out to be $120 \, \text{m s}^{-1}$. This value is consistent with predictions reported in the simulations (Dubs *et al.* 2011). Since the jet diameter is approximately $2 \, \text{mm}$, equation (2.1) also implies that the average mass density amounts to $\rho \approx 460 \, \text{kg m}^{-3}$, a fairly high value suggesting the presence of dense phases. From these estimates, the volumetric flow rate is $\dot{m}/\rho = 0.21 \text{s}^{-1}$ a value fully consistent with the characteristics of

the experimental setup provided by NitroCision (Ducos *et al.* 2008). Using a realistic equation of state for nitrogen (Lemmon *et al.* 2002), we then find that, for the inferred values of temperature and mass density, a homogeneous nitrogen jet should be hypercritical and the pressure should be of the order of 20 MPa. However, it is known from the present jet configuration that pressure is nearly atmospheric prior to impact. Hence, nitrogen in the jet needs to be in a heterogeneous state, involving several phases. Such heterogeneity should stem from nitrogen compressibility, interactions with the surrounding atmosphere and overall dissipation all along the free course of the jet. Obviously, a thorough sophisticated analysis is needed to characterize such heterogeneity. However, additional information on the structure of the jet will be provided below from inspection of jet-induced damage. Furthermore, the orders of magnitude provided by the present average analysis are useful information for the assessment of the interactions between the jet and the targeted material.

3. Experimental results

This section is devoted to the relationship between the mechanical properties of metallic materials and the damage patterns observed under the impact of the nitrogen jet. Part of these data was published earlier in Laribou *et al.* (2010*a*,*b*). Discussion and interpretation of these results follow in §4. Two groups of materials were selected for the tests: relatively soft materials and comparatively harder materials. The samples were rectangular $35 \times 22 \times 10\,\mathrm{mm}^3$ parallelepipeds whose surfaces were carefully mirror finished, down to a mean roughness value Ra less than $0.2\,\mu\mathrm{m}$.

The soft materials comprise the 1050A aluminium alloy (0.25%Si, 0.40%Fe, 0.05%Cu, tensile strength 76 MPa, yield stress 35 MPa, hardness 20–30 HV, density $2700\,\mathrm{kg\,m}^{-3}$) and OFHC copper (oxygen-free high conductivity) (99.95% Cu, minimum tensile strength 260 MPa, minimum yield strength 200 MPa, hardness 100 HV, density $8900\,\mathrm{kg\,m}^{-3}$). The stress versus strain curves obtained from tensile tests at low and room temperature are presented in figures 1 and 2, respectively (77 K was reached by installing the whole tensile device in a liquid nitrogen bath). Note that the ductility of the 1050 Al alloy decreases with temperature, and that the yield stress, although slightly increasing when temperature decreases, is still quite low. For OFHC copper, the yield stress becomes significantly higher at low temperature. The increase in the observed ductility cannot be regarded as significant, owing to the large dispersion in the ductility recorded at room temperature. The latter is owing to the presence of geometrical defects in our samples. The relatively hard materials include the bcc E24 low carbon mild steel (C < 0.06%, P < 0.015%, S < 0.05%, minimum tensile strength 420 MPa, minimum yield strength 320 MPa, hardness 150 HV, density $7710\,\mathrm{kg\,m}^{-3}$) and the fcc 316L (AISI321) austenitic stainless steel. The stress versus strain curves obtained from tensile tests at low and room temperature are presented in figure 3 for the E24 mild steel. Note the dramatic increase in the yield stress and decrease in ductility at low temperature suggesting that the ductile-to-brittle transition is reached above 77 K. The 316L austenitic stainless steel characteristics are: C < 0.06 per cent, Si < 0.75 per cent, Cr 16–18 per cent, Ni 10.5–12.5 per cent, Mo 2–2.5 per cent, minimum tensile strength 630 MPa,
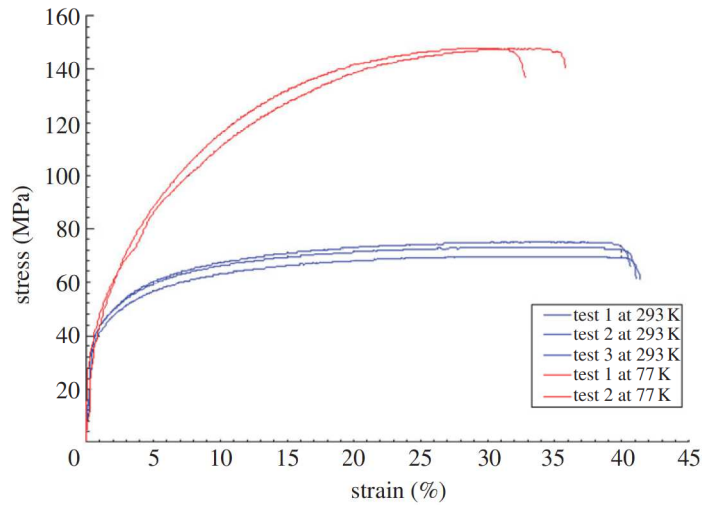
Figure 1. Stress versus strain curves of aluminium alloy 1050A at low and room temperatures. (Online version in colour.)
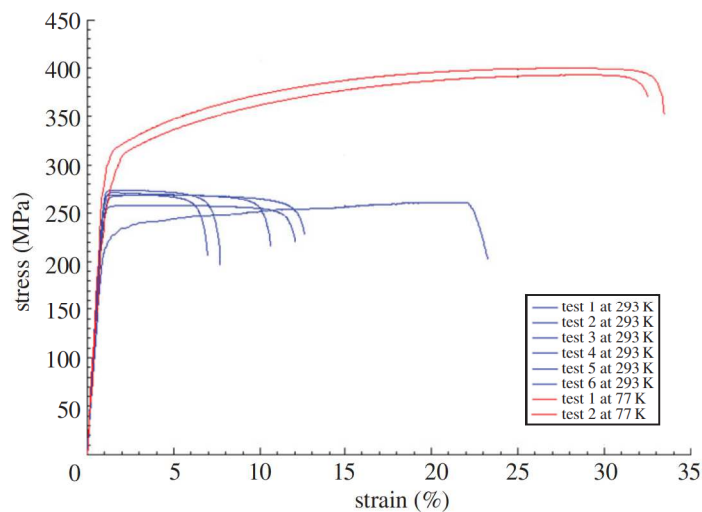

Figure 2. Stress versus strain curves of OFHC copper at low and room temperature. (Online version in colour.)

minimum yield strength $300\,\text{MPa}$, hardness $250\,\text{HV}$, density $7900\,\text{kg}\,\text{m}^{-3}$. The corresponding stress versus strain curves at low and room temperature are presented in figure 4. At low temperature, the yield stress is higher, no loss of ductility is observed and strain hardening is enhanced at large strains owing to a significant martensitic transformation that strengthens the material. It should be noticed that, with the exception of the bcc mild steel E24 at $77\,\text{K}$ (a temperature not reached in our jet experiments), ductility of the investigated materials is expected in the nitrogen jet conditions.
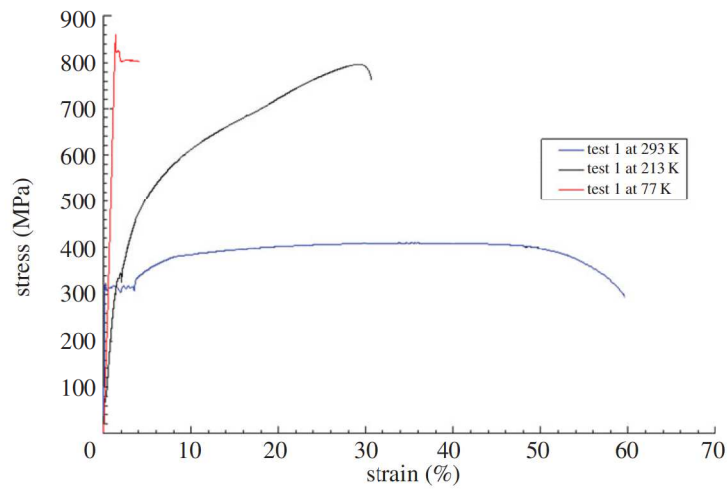
H. Laribou et al.

Figure 3. Stress versus strain curves of bcc mild steel E24 at low, medium and room temperatures.
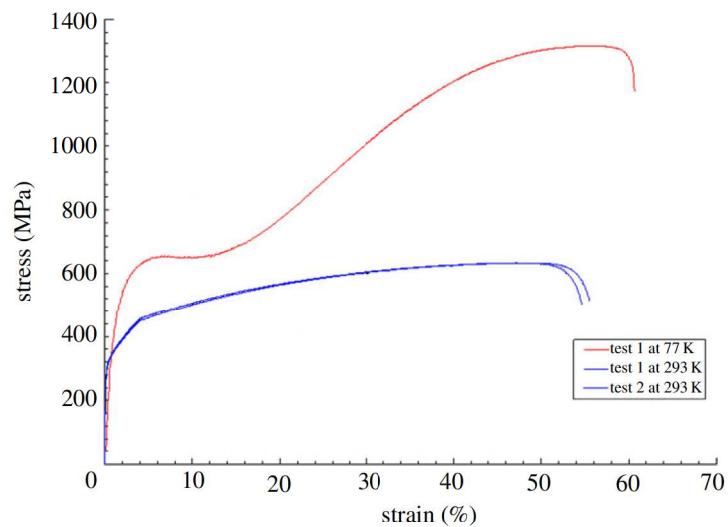(Online version in colour.)

Figure 4. Stress versus strain curves of fcc stainless steel 316L at low and room temperatures.
(Online version in colour.)

(a) Static point-wise tests: 1050A aluminium alloy and oxygen-free high conductivity copper

In a 'point-wise' test, a fixed point of the material surface is targeted. Alternatively, a linear transit of the jet over the surface may also be used in the following. Such 'dynamic tests' correspond to standard industrial use of the jet, where surface-treatment in some sense is the objective. Point-wise tests were employed to assess the evolution in time of damage, particularly in soft materials
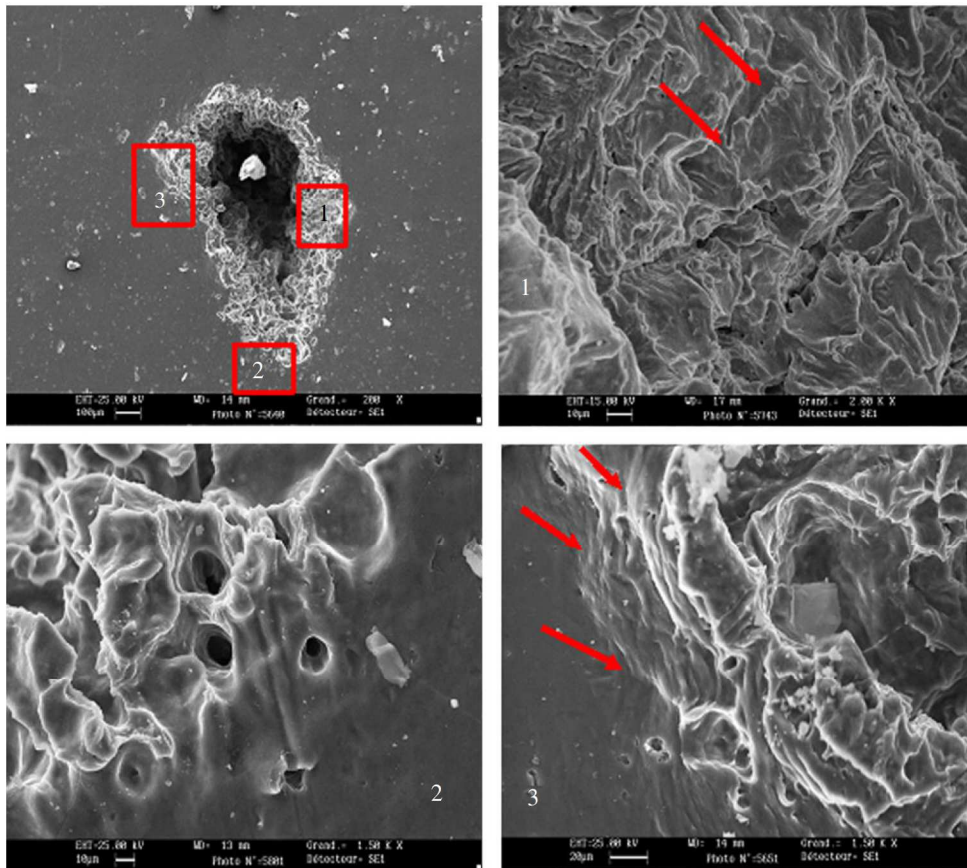
Figure 5. Crater in aluminium alloy 1050A in point-wise test for a dwell time of 1 s. Blow-ups in insets: (1) brittle fracture; (2) micro-cavities and (3) ripples of repelled matter and plastic slip lines at the crater's edge. (Online version in colour.)

where strong variations are expected. These tests were performed at the upstream pressure of 210 MPa, with a standoff distance of 60 mm, on the 1050A aluminium alloy and OFHC copper samples. The dwell time values: 1, 4, 8, 16, 32 and 60 s were used. The impacted area of the target was observed with an optical microscope allowing accurate depth measurements (3D InfiniteFocus Alicona) and a scanning electron microscope (SEM). As seen from the SEM micrographs in figures 5–7, craters were formed in less than 1 s in both materials, which suggests that local strain rates can be rather large, at least of the order of $1 \, \text{s}^{-1}$. The craters were deeper in the 1050A aluminium alloy (figure 7), which is consistent with the softer behaviour shown in figure 1. In this case, the width of the crater was approximately 0.5 mm in a dwell time of 1 s, and became 1.4 mm for a dwell time of 60 s. Several interaction mechanisms are evidenced in the insets of figure 5. Surprisingly, in inset 1 brittle fracture and cleavage patterns are observed. In inset 3, ripples of matter observed at the crater's rim rather suggest the occurrence of plastic deformation. Sometimes, superimposed
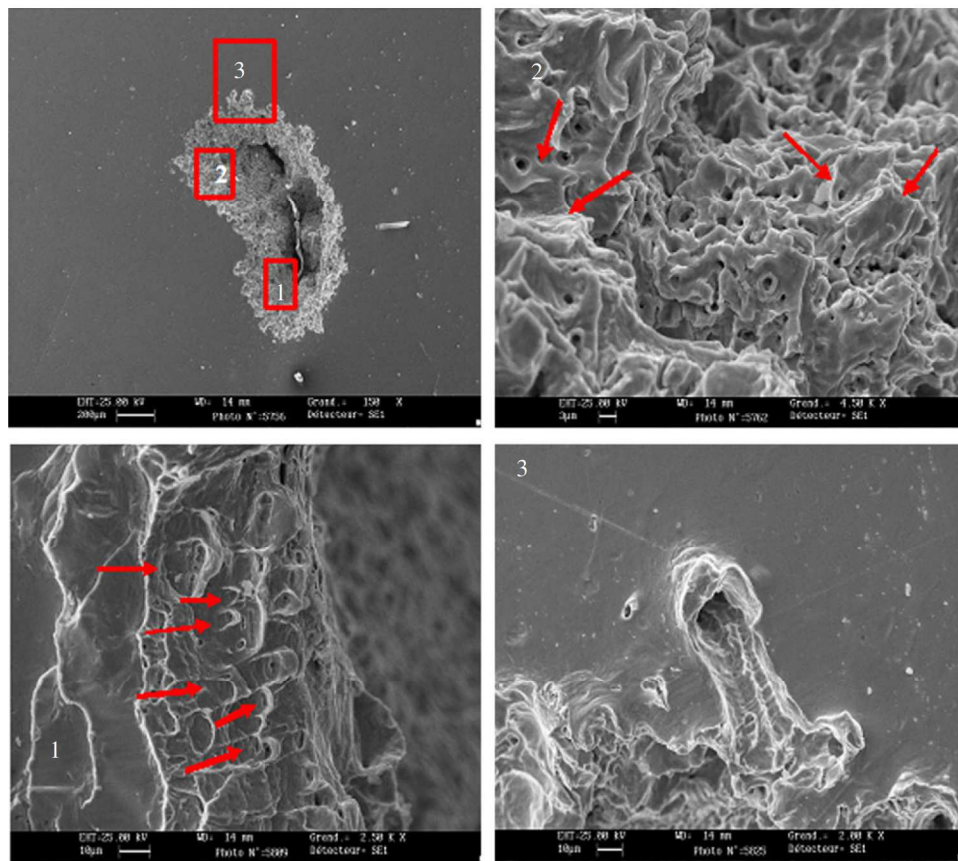
Figure 6. Crater in OFHC copper in point-wise test for a dwell time of 60 s. Blow-ups in insets: (1) plastic deformation; (2) brittle fracture combined with nucleation of micro-cavities and (3) groove formed at the crater's edge. (Online version in colour.)

on these somewhat contradicting figures, microcavities are additionally observed (inset 2). The crater produced in the copper target was hardly different (figure 6), although its depth was smaller as well as its width: 0.12 mm for a dwell time of 1 s and 0.47 mm for a dwell time of 60 s. For a 60 s dwell time, figure 6 (inset 1) suggests again a combination of superimposed damage mechanisms: cleavage and nucleation of microcavities. In addition, limited plastic deformation in the form of ripples of matter was observed at the edge of the crater (inset b). A channel and a vent suggesting the evacuation of confined gas is seen in inset 2. Figure 16 shows another occurrence of such vents in the 1050A alloy.

(b) Dynamic tests with a transiting jet: E24 mild steel and 316L stainless steel

The samples were manufactured, polished and tested under the following conditions: the operating pressure was 210 MPa and the transit speed 20 mm min^{-1}. Note that, owing to the width of the jet, its transit speed induced a local dwell time of 10 s, sufficient to cause a decrease in the local surface
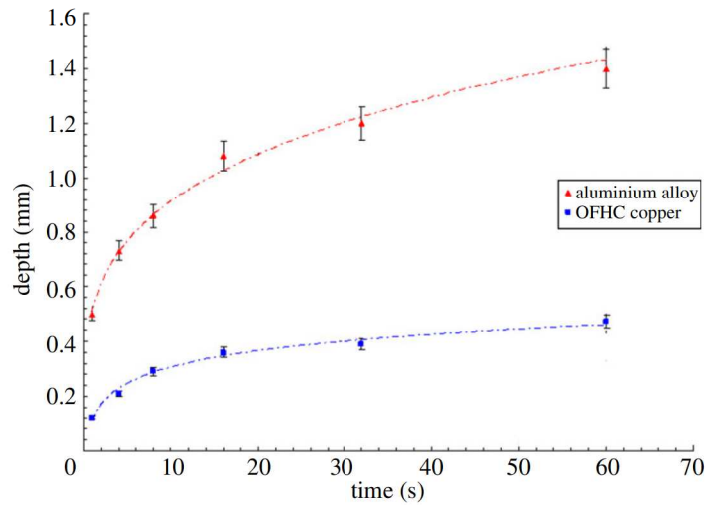
Figure 7. Crater depth evolution (mm) versus dwell-time (s) for aluminium alloy 1050A and OFHC copper at standoff distance of 60 mm (operating pressure is 210 MPa). (Online version in colour.)
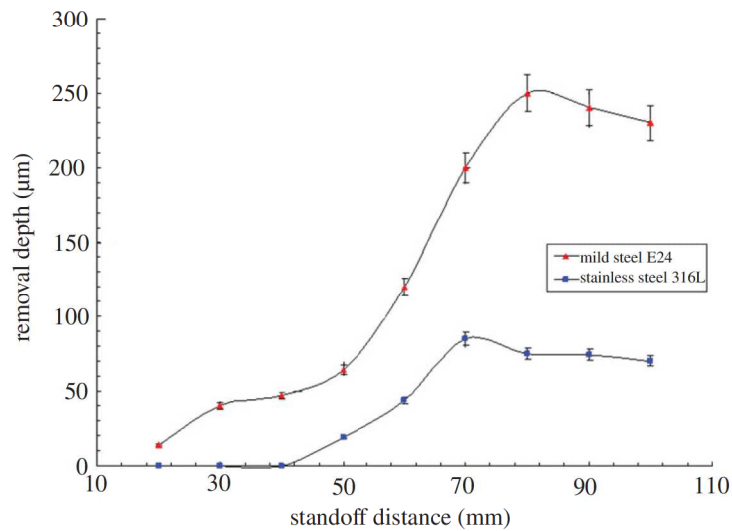
Figure 8. Removal depth (μm) versus standoff distance (mm) for E24 and 316L steels (operating pressure is 210 MPa). (Online version in colour.)

temperature of the sample to approximately 200 K. The standoff distance was varied from test to test, in the range 20–100 mm. The depth of matter removal is shown in figure 8. Cross-checking the data with figure 7 suggest that under similar dwell time and standoff distance (10 s, 60 mm), the depth of matter removal was about 50 times less in the stainless steel 316L than in the 1050A aluminium alloy. A few significant optical micrographs are also shown in figure 9 for the 316L steel and figure 10 for the E24 steel, respectively. The examination of the samples

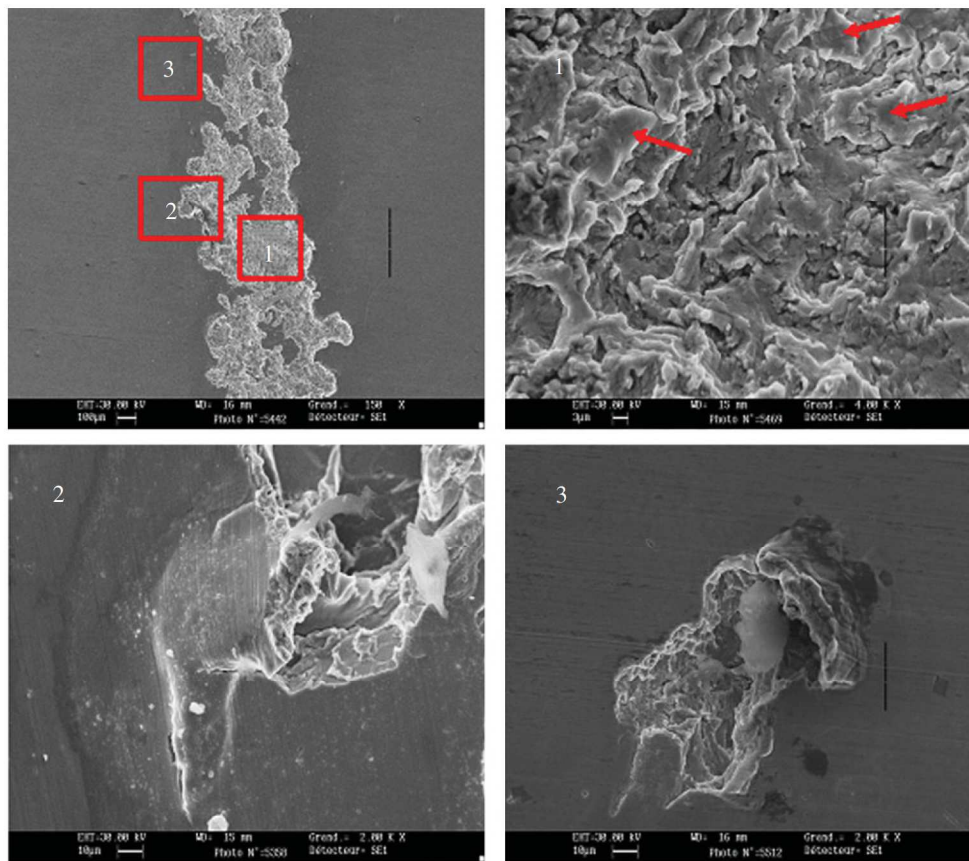Figure 9. Typical damage identified for 316L steel (for all standoff distances in the range 50–90 mm); Blow-ups in insets: (1) brittle fracture; (2) lifting of a chip at the edge of the groove; and (3) spalling. (Online version in colour.)

reveals that the jet does not have visible effects on these materials at small standoff distances (below 20 mm for E24 mild steel and up to 40 mm for 316L stainless steel, figures not shown). At larger standoff distances (approximately beyond 50 mm), the depth measurements indicate a significant difference between these two steels. Figures 8–10 suggest that the nitrogen jet has a much greater effect on the E24 mild steel than on the 316L stainless steel, and that the jet is not equally efficient for matter removal over its impact width. The damage is mainly localized in its central part. Beyond 90–100 mm standoff, matter removal decreases quickly. The observed correlations between the standoff distance and the surface damage patterns suggest the presence in the jet of dense (hypercritical or liquid) phases in the range of standoff distances 50–100 mm. Below 20 mm, the jet is unable to inflict damage to the impacted surface and is therefore conjectured as being gaseous. Beyond 100 mm standoff distance, the jet structure becomes loose, and as its width increases, its growing interactions with the surrounding atmosphere curtail its performances.

Figure 10. Typical damage identified in mild steel E24 (for all standoff distances in the range 50–100 mm). Blow-ups in insets: (1) intergranular fracture by cleavage; (2) cracking at the crater's edge and (3) interconnected network of micro-cracks. (Online version in colour.)

SEM observations were carried out in both materials. Two types of damage were identified in the 316L stainless steel, depending on the standoff distance: a continuously lightly damaged groove, only visible through a different contrast from the rest of the surface, was observed at small and large standoff distances (below 40 mm and beyond 100 mm), and discontinuously damaged spots, of depth approximately 100 µm, for standoff distances in this range. In figure 9 (inset 1), facets reminiscent of brittle fracture are seen rather than ductile dimples, with a rather homogeneous distribution across the groove, although figure 9 (inset 2) suggests increased intensity of the impact at the edge of the groove. Spalling was also identified in individual impacts scattered around the course of the jet as shown by figure 9 (inset 3).

The E24 mild steel presents quite similar, but more spectacular, damage modes (figure 10). For a standoff distance of 20 mm, no damage was observed except at the edges of the target where a rather consequent removal of matter is identified. For a standoff distance of 30 and 40 mm, the observed damage is discontinuous and irregular along the course of the jet, with a more substantial
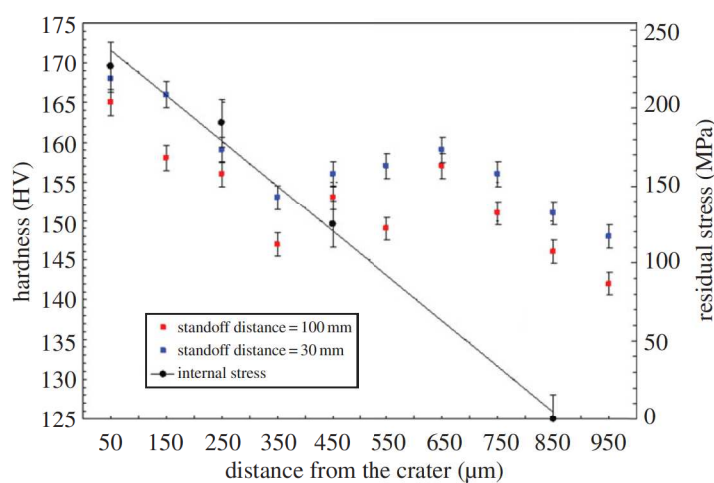
Figure 11. Hardness and internal stress versus distance from groove in mild steel E24. The sign of internal stress was changed for convenience (they are compression stresses). Error bars are added. (Online version in colour.)

removal of matter at the edges of the target. For a standoff distance in the range 50–100 mm, the jet marks out an irregular and continuous groove. The SEM observations of the groove in this range (figure 10) reveals: (inset 1) a central zone exhibiting intergranular brittle fracture by cleavage, (insets 2 and 3) two side zones showing various forms of damage, microcracking, (inset 2) as well as a network of interconnected cracks (inset 3). To investigate a possible correlation between the damage patterns and the microstructure of material, the samples were observed after chemical etching with a 5 per cent Nital solution (figure not shown). In the various observations carried out, evidence of such a correlation is unclear and the damage patterns seem to be independent of the microstructure.

Measurements of the microhardness in the neighbourhood of the jet groove were performed, using a ZWICK ZHV1/2 Vickers microdurometer. It is seen in figure 11 that, next to the groove in the mild steel E24, microhardness increases significantly above the average value of 150 HV observed in the absence of jet treatment. This average value is recovered 800 to 1000 μm away from the groove. We note that varying the standoff distance from 30 to 100 mm does not alter significantly these results, although the crater depth is larger in the second case. X-Ray diffraction residual stress measurements performed inside the jet affected zone are also shown in this figure (the $\sin^2\psi$ method was used); all the values are given with an uncertainty of the order of ±20 MPa. They reveal that compressive residual stresses are present in this area. Hence, the increase in microhardness can be correlated with residual stress building. To unravel the possible mechanisms for such a surface hardening effect, in-depth electron backscatter diffraction (EBSD) observation of the area located below the groove were carried out, as well as chemical measurements of the nitrogen concentration. Indeed, we note that dissociative adsorption of nitrogen as provided by the jet easily takes place on Fe surfaces at the attained temperatures (Ertl *et al.* 1982). A Leica S440 was used for SEM and EBSD investigations; the samples were cut perpendicular to the
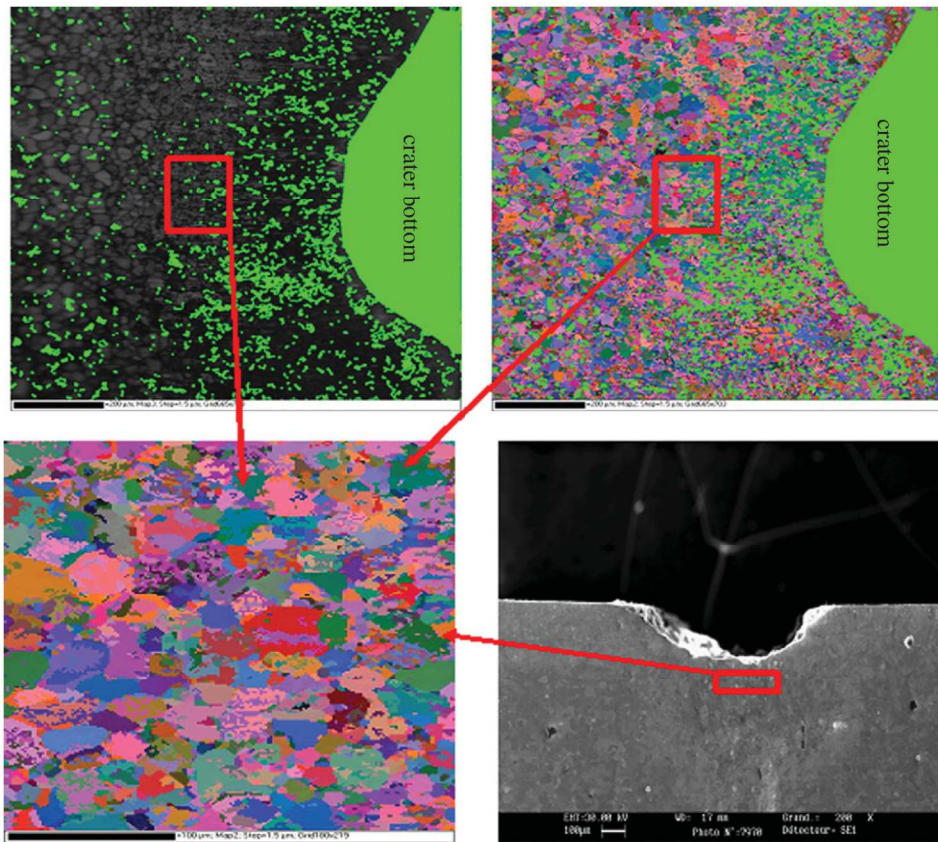
Figure 12. Grain fragmentation in mild steel E24 below the crater. All insets show the same area. Indexing quality index is upper-left, un-indexed areas are shown in green in upper-left and right views. (Online version in colour.)

groove. The section was carefully polished and chemically etched with a 5 per cent Nital solution. Grains were identified based on a 10° disorientation criterion using the EBSD technique. Figure 12 shows a picture of the microstructure observed in the E24 mild steel below the groove. The jet-affected area can be identified from the grain size, which decreases from an average 30 μm away from the jet impact area to less than 5 μm in the jet-affected zone. The latter extends down to 600 μm below the bottom of the groove. As figure 13 shows, the grain refinement goes along with a significant increase in the hardness of the material, down to 350–400 μm below the surface. The grain size reduction seems to be obtained by grain fragmentation. Indeed, just below the surface, the microstructure is essentially crushed and a great indexing difficulty was encountered. The reduction of the grain size is obtained without significant plastic strain, and no texture development could be identified (figure not shown). In the case of 316L stainless steel sample, no significant change in the microstructure after the jet impact could be noticed from the EBSD observations. Unlike the mild steel case, no reduction of the grain size was observed, although some grain fragmentation was noticed
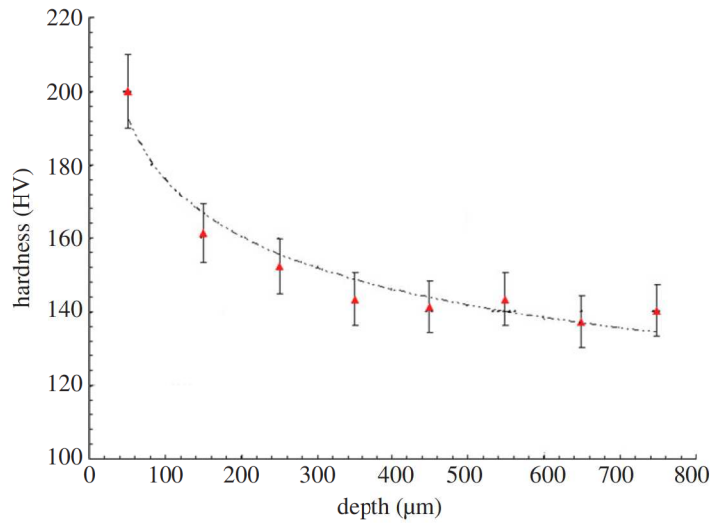
Figure 13. Hardness measurement under the groove in mild steel E24. The average hardness in the absence of a jet impact is 150 Vickers. Error bars are added. (Online version in colour.)

below the surface. This might be an earlier stage of the phenomenon observed in the E24 mild steel, but a local martensitic transformation might additionally take place at low temperature. However, this possibility was not checked in the present investigation.

As already mentioned, insertion of nitrogen atoms in Fe crystals occurs through a dissociative adsorption mechanism at low temperatures ($-110°C$) (Ertl *et al.* 1982). The interatomic links of N_2 molecules (which become gaseous at the contact of the surface) are weakened, and the activation energy required for breakage is significantly reduced. Thus, the nitrogen molecules can be entirely dissociated at the surface to provide atomic nitrogen. Measurements of the in-depth nitrogen atomic concentration in the mild steel E24 were subsequently carried out using a Jeol 7001FLV FEG equipped with an Oxford INCA Wave 700 WDS. A LSM-80E crystal was used for nitrogen detection and quantification with a very high probe current. Several standards with different nitrogen volume fractions enabled a complete calibration to be made for an optimum determination. In these conditions, a profile was obtained in the thickness of the sample, showing a substantial transport of nitrogen atoms to depths of the order of $100\,\mu m$ where the nominal nitrogen content is reached (figure 14). More accurate measurements in a restricted area (down to $50\,\mu m$) indicate a weight concentration of the order of 0.02 per cent, or an equivalent atomic concentration of 0.08 per cent (figure 14, Inset). Despite a rather short dwell time (approx. $10\,s$), this concentration is hardly lower than that obtained from plasma nitriding for several hours at high temperature ($400°C$) in bcc materials. Furthermore, the penetration depth of nitrogen is much larger than that reached by using plasma nitridation, as the latter typically amounts to a few micrometers (Murakami *et al.* 2005). Hence, ultra-fast transport of nitrogen atoms in the depth of the material can be inferred from these observations. Owing to the low temperatures induced by the jet, diffusion should be ruled out as a transport mechanism. Because grain
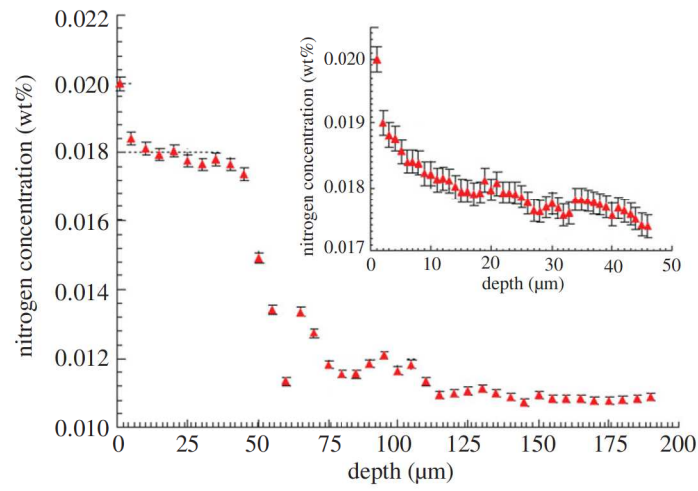
Figure 14. Profile of nitrogen concentrated (wt%) versus depth (micrometres) in mild steel E24 on 200 μm of depth below the crater. Inset: Profile on 50 μm of depth below the crater. Error bars are added. (Online version in colour.)
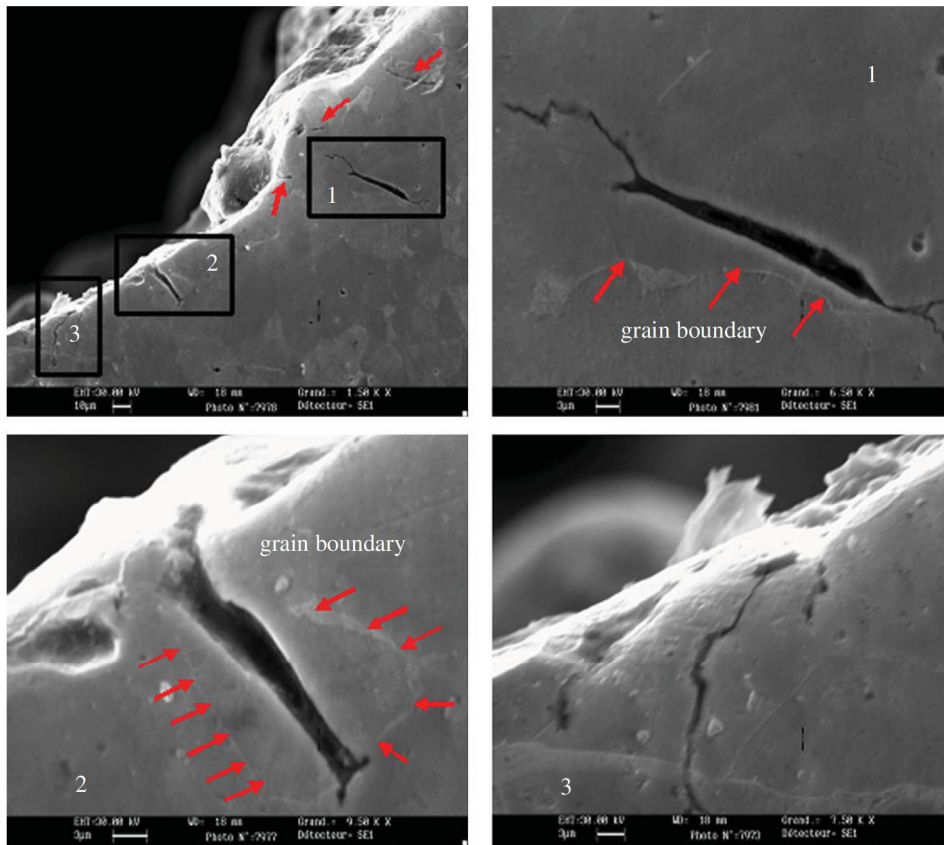

Figure 15. SEM observations below the crater in E24 steel after Nital 5% etching, showing crack propagation into the material. Blow-ups in insets 1, 2 and 3. (Online version in colour.)

fragmentation was observed in the impacted area, we conjecture instead that the paths for ultra-fast transport belong to the resulting network of cracks (figure 15), which pertain to the incorrectly indexed area in the above EBSD analyses. The insertion of nitrogen atoms in the lattice helps explain the compressive character of the measured residual stresses. It may also contribute to explaining the presence of cleavage fracture at low temperature in the fcc 316L stainless steel, in spite of the ductile behaviour reported in figure 4 (Defilippi *et al.* 1969).

4. Discussion: probing into the mechanisms of nitrogen jet/metallic material interaction

The various surface patterns and microstructural transformations revealed by the observations of the previous section raise numerous questions as to what the mechanisms for the jet/surface interactions are. As suggested in our micrographs, several mechanisms may combine and sometimes overlap in space to create amazingly complex damage patterns. In this section, our intent is to identify the interaction mechanisms at work in our experiments, and to justify our conjectures by estimating the loading parameter values they involve (stress, strain rate, temperature, etc.).

We start with two mechanisms inducing plasticity of the targeted material, as illustrated in figure 5 (inset 2), figure 6 (inset 2) and figure 16, which we call the 'blistering' and 'blasting' effects. Let us assume that a mass m of dense nitrogen phases penetrates the target through some cracks and finds itself confined in a cavity of volume V, where it rapidly warms up to the ambient temperature level T. It then becomes gaseous and the confinement hydrostatic pressure rapidly increases. Its value can be directly obtained if the standard pressure–volume–temperature dependence is assumed for the nitrogen gas:

$$PV = mRT.$$

Here, m is the quantity of nitrogen confined in the volume V: in other words, the mass-density of nitrogen in its average dense phase, which we found to be of the order of $460 \, \mathrm{kg \, m^{-3}}$. R is the universal gas constant ($296.8 \, \mathrm{J \, kg^{-1} \, K^{-1}}$), and T the ambient temperature. We, therefore, find hydrostatic pressures of the order of $40 \, \mathrm{MPa}$, possibly rising up to $120 \, \mathrm{MPa}$ for liquid nitrogen, sufficient to induce growth of the microcavities and bursts of gas through the cavity wall. As an illustration of this blistering mechanism, we include in figure 16 the portrait of a channel and a vent clearly revealing the passage of confined gas in the 1050A aluminium alloy. Note that blistering can be enhanced by pre-heating the material surface before the impact of the jet. The blasting effect occurs in a quite similar fashion. The constant mass inflow (of the order of $90 \, \mathrm{g \, s^{-1}}$) of the dense nitrogen jet into, say, a crater in a point-wise test, induces a very significant volumetric outflow of nitrogen gas (approx. $75 \, \mathrm{l \, s^{-1}}$) owing to rapid warm up of nitrogen during the interaction with the target at room temperature. Pressures of the order of $100 \, \mathrm{MPa}$ are similarly expectable, sufficient to repel matter at the rims of the crater by local plastic deformation.

However, plastic deformation does not seem to be the main phenomenon in the present investigation. The general rule seems to be elastic-brittle behaviour. Brittleness can indeed be expected from the bcc E24 mild steel at low
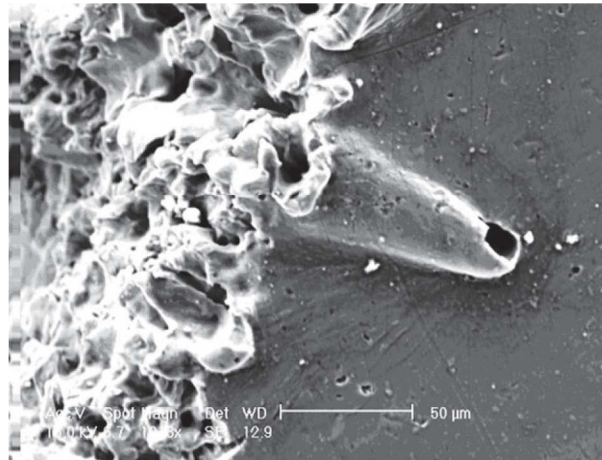
Figure 16. Portrait of a channel and a vent revealing passage of confined gas in the aluminium alloy 1050A at the crater's edge (Courtesy P. Brenot, CRITT M2T).

temperatures, as figure 3 testifies, all the more so that relatively high local strain rates in the damaged areas (estimated earlier at approx. $1\,\mathrm{s}^{-1}$) contribute to increasing the brittle-to-ductile temperature. However, metals and alloys with fcc lattice are usually ductile over the whole temperature range, as illustrated in figures 1, 2 and 4. Several reasons may be found for such a brittle behaviour in our fcc samples in jet conditions: (i) As already mentioned, the insertion of nitrogen atoms in the lattice could promote cleavage fracture in the fcc 316L stainless steel and (ii) figure 12 suggests that the brittleness may be because of thorough penetration of the dense nitrogen phases in the bulk of the material through a network of cracks. Crack growth may then occur through blasting, but in addition, owing to thermoelastic properties, the sudden temperature drop induces tensile stress waves propagating into the material. We show below that the stress levels obtained in this manner may reach rather high values, able to sustain crack growth. In this interpretation, grain fragmentation below the crater is driven by a combination of fast thermoelastic contraction, dislocation motion hampering and blasting induced by the thermal shock.

To obtain orders of magnitude for the peak tensile stress, the problem is simplified into the one-dimensional sudden cooling of a thermoelastic half space. Two models (Singh 1967; Fressengeas & Molinari 1980) were used to estimate the tensile stress induced by the thermal shock in a direction normal to the surface. The models differ on the assumed mechanism for the inflow of energy in the material. In the work of Singh (1967), surface input by heat conduction is assumed: the body initially at rest is suddenly subjected on its edge to a constant (negative) heat flux. In the work of Fressengeas & Molinari (1980), the heat inflow occurs through radiation and volumetric input in a thin layer below the surface. These volumetric conditions seem to be more realistic in the present problem. However, when the width of the layer nears zero, a surface input is recovered. Concurrently using these two models allows freeing our estimates from any particular assumption on the input of energy. In the Cartesian reference

frame, the body lies in the half space $x \geq 0$. Any motion is perpendicular to the plan $x = 0$, which coincides with the surface. The displacements are therefore: $u_y = u_z = 0$ and $u_x = u(x, t)$. Consistently, the relative temperature field is taken in the form: $T = T(x, t)$. In a first-order approximation neglecting part of the thermomechanical coupling, the fundamental equations for a linear thermoelastic problem can be written as

$$\rho \frac{\partial^2 \varepsilon}{\partial t^2} = \frac{\partial^2 \sigma}{\partial x^2},$$

$$\sigma = (\lambda + 2\mu)\varepsilon - \beta T$$

and

$$\rho C \frac{\partial T}{\partial t} = k \frac{\partial^2 T}{\partial x^2} + P.$$

In the balance of momentum, ρ is the mass density, σ the stress and ε the strain, λ and μ are the isothermal Lamé constants, β the thermal expansion coefficient, C the specific heat, k the thermal conductivity. P denotes a volumetric energy density input per unit time. The body is initially at zero (relative) temperature: $T = 0$, $t \leq 0$, $x \geq 0$ and its surface is suddenly cooled down. In the model (Singh 1967), cooling occurs with the constant heat flux q: $-k \partial T / \partial x = q H(t)$, $x = 0$, $t \geq 0$, where H is the Heaviside unit step function, and the volumetric energy input P is zero. In the model (Fressengeas & Molinari 1980), the volumetric energy input is taken in the form: $P = (A/x_p)e^{-x/x_p} H(t)$, where x_p is the depth of penetration of the energy in the body and A is a constant, but the conductive heat flux q is equal to zero. In both models (Singh 1967; Fressengeas & Molinari 1980), closed form solutions to this system of partial differential equations are obtained from regular perturbation methods. For $q < 0$ and $P < 0$, the first-order solutions show the existence of a tensile stress wave propagating through the body. It can be shown from these results that a first-order estimate of the maximum stress resulting from either model is, when the penetration depth x_p is small enough: $\sigma_{\max} = \beta q / \rho C V = A\beta / CV$, where $V = \sqrt{(\lambda + 2\mu)/\rho}$ is the velocity of elastic waves. Further, the raising time T needed to reach this value is approximately: $T \cong 8 k / \rho C V^2$. Using the heat flux value $q = 5 \times 10^8 \, \text{W m}^{-2}$ and the data for the E24 mild steel $\rho = 7800 \, \text{kg m}^{-3}$, $V = 5835 \, \text{m s}^{-1}$, $\beta = -500 \, \text{MPa K}^{-1}$, $k = 54 \, \text{W (m K}^{-1})$ and $C = 300 \, \text{J (kg K}^{-1})$, an estimate of the maximum tensile stress obtained from this relation is 55 MPa. The raising time is extremely short. Assisted by the blasting effect, the resulting stress and strain rate seem to be large enough to contribute to crack initiation parallel to the free surface.

5. Conclusions

A cryogenic nitrogen jet was used to impact the surface of metallic materials. Estimates for the physical parameters characterizing the jet in the impacted area (temperature, pressure, phase composition, mass density) were derived from simple experiments. Depending on the material and test parameters (standoff distance, dwell time, upstream vessel pressure), the jet/surface interaction modes included cleavage, spalling, blistering, crack nucleation and growth, grain fragmentation and ductile deformation. These modes may be superposed in the

same test, or even in the same material area. Despite information gathered in conventional cryogenic testing suggesting the possibility of ductile behaviour at low temperature in all materials (except perhaps in a bcc steel), the brittle modes prevailed under the jet impact, owing to thermomechanical shock conditions. Estimates of the involved stress and strain rates were produced, based on thermomechanical interpretations. Surface hardening in a rather deep layer was found to be correlated with grain fragmentation, the existence of a compressive residual stress state and ultrafast transport of dissociatively adsorbed nitrogen at large depths in the material.

References

Defilippi, J. D., Brickner, K. G. & Gilbert, E. M. 1969 Ductile-to-brittle transition in austenitic chromium-manganese-nitrogen stainless steels. *Trans. Metall. Soc. AIME* **245**, 2141–2148.

Dreitser, G. A., Firsov, V. P., Antyukhov, I. V. & Morozov, D. A. 2001 The interaction of a liquid nitrogen jet with a surface in boiling. *Heat Transfer Res.* **32**, 84–90.

Dubs, P., Khalij, M., Benelmir, R. & Tazibt, A. 2011 Study on the dynamical characteristics of a supersonic high pressure ratio underexpanded impinging ideal gas jet through numerical simulations. *Mech. Res. Commun.* **38**, 267–273. (doi:10.1016/j.mechrescom.2011.02.016)

Ducos, M. D., Richard, F., Matile, O., Warnecke, R., Hume, H. & Debionne, T. 2008 New LN2 cryogenic process to strip parts thermal spray coated. In *Int. Thermal Spray Conf. and Exposition: Thermal Spray Crossing Borders* (*DVS-ASM*), pp. 695–700.

Ertl, G., Lee, S. B. & Weiss, M. 1982 Kinetics of nitrogen adsorption on Fe (111). *Surf. Sci.* **114**, 512–526. (doi:10.1016/0039-6028(82)90702-6)

Fressengeas, C. & Molinari, A. 1980 Transient stress induced by thermal shock. *J. Thermal Stresses* **3**, 379–390. (doi:10.1080/01495738008926976)

Laribou H., Fressengeas C., Entemeyer D., Jeanclaude V. & Tazibt A. 2010*a* Surface damage and treatment by impact of a low temperature nitrogen jet. In *Int. Conf. on Advances in Materials and Processing Technologies* (eds F. Chinesta, Y. Chastel & M. El Mansori), vol. 1315, pp. 1222–1227. PTS I and II Book Series. Paris, France: AIP Conference Proceedings.

Laribou H., Fressengeas C., Entemeyer D., Jeanclaude V. & Tazibt A. 2010*b* Surface damage by impact of nitrogen jet under high pressure and low temperature. In *Supplemental Proc. on Materials Processing and Properties, Vol 1: Materials Processing and Properties*, Seattle, WA, pp. 627–634. Seattle, WA.

Lemmon, E. W., Huber, M. L. & McLinden, M. O. 2002 NIST Standard Reference Database 23: Reference Fluid Thermodynamic and Transport Properties-REFPROP, v. 7.0. Gaithersburg, MD: National Institute of Standards and Technology. Standard Reference Data Program.

Murakami, K., Nishida, N., Osamura, K., Tomota, Y. & Suzuki, T. 2005 Plasma nitridation of aluminized high purity iron. *Acta Mater.* **53**, 2563–2579. (doi:10.1016/j.actamat.2005.02.014)

Singh, D. V. 1967 Thermal stress in a semi-infinite medium due to constant heat flux at the surface. *Arch. Budowy Masz.* **14**, 65–72.